Key Engineering Materials Vols. 153-154 (1998) pp. 301-323

Sintering and Densification; New Techniques: Sinter Forging

A.J.A. Winnubst[1] and M.M.R. Boutz[2]

[1] University of Twente, Faculty of Chemical Technology, Laboratory for Inorganic Materials Science, P.O. Box 217, NL-7500 AE Enschede, The Netherlands

[2] TU Hamburg-Harburg, Advanced Ceramics Group, P.O. Box 901052, D-21071 Hamburg, Germany

Keywords: Sintering, Densification, Sinter Forging, Creep, Hot Pressing, Hot Isostatic Pressing, Stress Multiplication, Constitutive Equations, Kinetics, Properties, Microstructure

Abstract

In this chapter pressure assisted sintering methods will be described. Attention will mainly be paid to sinter forging as a die-wall free uniaxial pressure sintering technique, where large creep strains are possible. Sinter forging is an effective tool to reduce sintering temperature and time and to obtain a nearly theoretically dense ceramic. In this way grain size in tetragonal zirconia ceramics can be reduced down to 100 nm. Another important phenomenon is the reduction of the number density and size of cracks and flaws resulting in higher strength and improved reliability, which is of utmost importance for engineering ceramics. The creep deformation during sinter forging causes a rearrangement of the grains resulting in a reduction of interatomic spaces between grains, while grain boundary (glassy) phases can be removed. The toughness and in some cases the wear resistance is enhanced after sinter forging as a result of the grain-boundary-morphology improvement.

1. Introduction

The intrinsic driving force for sintering is minimisation of the surface energy, particularly by the elimination of the free surface. This driving forces is often represented by the so-called sintering stress, which is inversely proportional to both particle size and pore radius [1]. The application of an external stress acts as an additional driving force for densification, especially when this external stress exceeds the intrinsic sintering stress [2]. The introduction of this additional driving force is one aspect of the use of pressure-assisted sintering techniques. Another reason for using these methods is the elimination of processing flaws in the sintered product. The densification and strength of sintered ceramics are often limited by processing defects arising from inhomogeneities in the powder compact after green forming e.g caused by the presence of agglomerates. Regions with different density densify at different rate which in turn leads to transient stresses, causes crack-like pores or large voids [3]. Differences in sintering rate within the compact is also possible in two-phase ceramic/ceramic composites where phases densify at different temperatures. These processes consequently limit densification and a homogeneous evolution of the microstructure [4]. These processing flaws can be removed by applying large shear strains, which can be achieved by applying an external stress on the compact during sintering [5,6].

Pressure-assisted sintering techniques can be divided into three main types:

1. Hot isostatic pressing (HIPing). Here a hydrostatic gas pressure is applied to the specimen and the shrinkage is isotropic. This technique is mostly applied to remove residual porosity (< 7 vol%), which has remained after free sintering. It is interesting for post-densification of complex shapes. Reducing gas atmospheres are used, which can give problems for HIPing metal oxide ceramic systems. Encapsulated HIPing has the advantage that green samples can be directly densified without a presintering treatment, but it is not widely used for ceramics because of several disadvantages related to the encapsulating step.

2. Hot pressing. A uniaxial pressure is applied to a powder, which is constrained in the lateral direction by a die wall. Hot pressing is commonly performed with inexpensive graphite dies and rams, which however necessitates an inert atmosphere (N_2 or noble gases) and is therefore not very useful for oxidic ceramics. This technique is commonly used to promote densification of inert, covalent materials like nitrides and carbides or composite materials, in which large differences in sinterability exists between the different phases
3. Sinter forging. A uniaxial pressure is applied to a partially dense sample, which is free to move in the lateral direction because of the absence of a die wall. Densification at a lower temperature can take place by sinter forging compared to free sintering. This can also result in a smaller grain size if no dynamic (strain-induced) grain growth occurs. Standard high temperature testing machines can be used and there is no necessity for an inert atmosphere. Only relatively simple (plate-shaped) forms can be made in this way.

In the next section the different processing paths for these pressure assisted sintering techniques will first be given. In this chapter on new sintering techniques further mainly attention will be paid to sinter forging as the most promising and economically interesting technique for improved sintering.

2. Processing paths for pressure sintering techniques

Fig.1 illustrates the processing paths (after [5]) for cylindrical specimens in terms of axial (ε_z) and radial (ε_r) strain for free sintering and the pressure sintering methods mentioned in the introduction. All paths are confined by three lines; i.e. the isotropic shrinkage line $\varepsilon_r = \varepsilon_z$ and the isodensity curves, defined by no densification ($\varepsilon_v = 2\varepsilon_r + \varepsilon_z = 0$) and full densification ($\varepsilon_v = \ln\{\rho_{th}/\rho_g\}$ with ρ_{th} the theoretical and ρ_g the green density). During free sintering and HIPing isotropic shrinkage occurs: ε_z equals ε_r and both are negative. During hot pressing ε_r is zero and the volumetric strain (ε_v) is equal to the axial strain and therefore the increase in density during hot pressing can be directly calculated from the axial displacement. Only in the case of sinter forging, the processing path is not fixed and depends on the applied stress. The sign of the radial strain depends on the relative magnitudes of sintering, which alone would lead to radial contraction, and creep, which alone would lead to radial expansion. At very low stresses ε_r is negative, while at higher stresses it becomes positive. To calculate the volumetric strain and hence the increase in density during testing necessitates the use of radial displacement transducers or the performance of interrupted tests.

The creep strain ε_c is the strain which occurs without any change in volume. For uniaxial deformation of cylindrical samples the creep strain ε_c as given by [7] is:

$$\varepsilon_c = \left|\varepsilon_z - (\varepsilon_v / 3)\right| = \frac{2}{3}\left|\varepsilon_z - \varepsilon_r\right| \qquad (1)$$

The second method to represent the different processing paths is to plot the volumetric versus the creep strain (after [5]) as shown in Fig.2. The processing paths are again confined to the region between the isodensity curves for no and full densification. During free sintering no creep occurs. HIPing also gives no macroscopic creep. However in this case local shear stresses and strains can occur within the sample. During hot pressing ($\varepsilon_r = 0$) the creep and volumetric strain are in a fixed ratio to each other:

$$-\varepsilon_v = \left|\varepsilon_z\right| = \frac{3}{2}\varepsilon_c \qquad (2)$$

Again, only for sinter forging the processing path is not a straight line. The creep strain of a material upon reaching its final density can be manipulated by the applied stress. This offers the opportunity to impose large creep strains on the material during densification. The application of such strains leads to an elimination of residual strength-limiting flaws as has been demonstrated both experimentally [5,8] and theoretically [9].

Increasing the ratio of creep strain to volumetric strain ($\varepsilon_c/\varepsilon_v$) during sinter forging is only possible if the compressive ductility of the material is sufficiently large under the thermomechanical conditions used. The ductility in compression of the new generation of fine-grained (< 1 μm), superplastic ceramics is very high and permits compression to strains larger than 1 (63% height reduction) without edge cracking. The ductility depends critically on microstructure. It decreases amongst other factors with increasing grain size [10], broadening grain size distribution [11] and increasing glass phase content above a critical concentration [12]. Attempts to sinter-forge coarse-grained ceramics were unsuccessful in the past [13] due to their limited ductility. In fact, both the first publications on ceramic superplasticity [14] and sinter forging ceramic components to large strains [15, 16] appeared about 10 years ago.

One drawback of sinter forging is that after reaching a certain density a transition to pure creep may occur under certain conditions. This transition occurs at 93 - 96% relative density, as observed both for Y-TZP samples [17, 18] and zirconia dispersed alumina [19]. The processing paths then proceed along an isodensity line. This is not the case for hot pressing, where any axial displacement leads to densification and the test can be ended once the material ceases to displace axially.

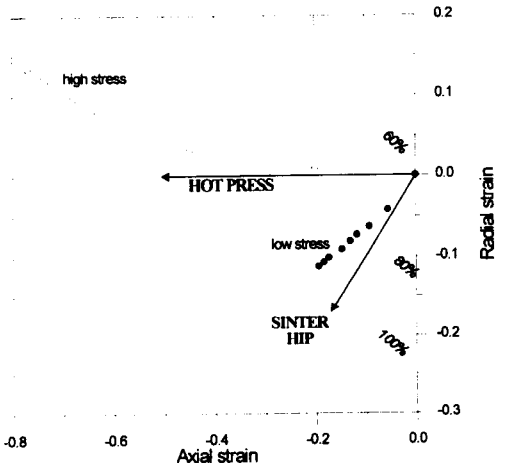

Fig. 1. Radial strain versus axial strain for different sintering techniques (after [[5]). Compare high and low stress paths for sinter forging.

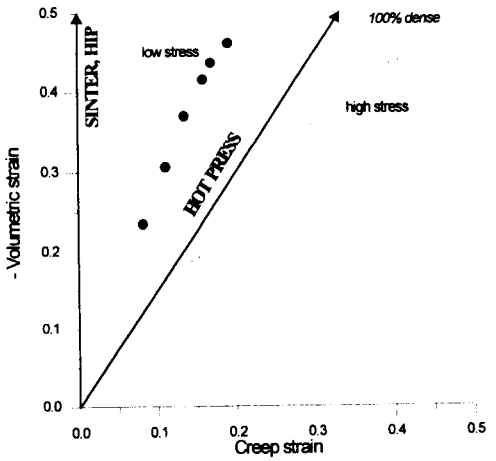

Fig. 2. Volumetric (i.e. densification) strain versus axial strain for different sintering techniques (after [5]). Again, only for sinter forging the path is not fixed.

3. The stress multiplication factor

3.1. Model considerations.

During pressure sintering the effective hydrostatic or mean stress is the sum of three terms: a term often referred to as the sintering stress (σ_s), that accounts for the surface tension forces of the curved pore surfaces, a term representing the internal pressure (p_i) of entrapped gases in closed pores and a term representing the local stress acting on grain boundaries. The term p_i only becomes important at the very end of sintering, when shrinkage of closed pores leads to the development of high pressures caused by entrapped, insoluble gases. The magnitude of the sintering stress is of the order of 1 MPa [16, 20] and can be neglected for the stresses, normally applied during pressure sintering. It is therefore the local grain boundary stress that dominates the effective hydrostatic stress. The effective stress thus equals the local stress and is related to the applied macroscopic stress (σ_a) by the stress multiplication factor ϕ:

$$\sigma_{eff} = \phi\sigma_a \tag{3}$$

The stress multiplication factor accounts for the reduction in internal load bearing area due to the presence of porosity. Numerous models have been proposed to describe the dependence of ϕ on porosity. As outlined by Funkenbush *et al.* [21], two general classes can be distinguished: (i) porosity-based and (ii) contact models. The resulting equations range from exponential [22] to linear [23] porosity-dependencies and are very similar to those used to describe the porosity-dependence of Young's modulus.

In the porosity-based models the stress multiplication factor is defined as the ratio of the total grain surface area (consisting of the total grain contact area plus the area occupied by porosity located between individual grains) to the actual load-bearing contact area. Various linear relationships have been proposed [23], yielding values for ϕ decreasing from 2 - 3 to 1 as porosity decreases from 50% to zero. However, Coble [23] demonstrated that of the various relationships, the only form consistent with steady-state diffusion models is given by:

$$\phi = 1/\rho = 1/(1-P) \tag{4}$$

where P is the fractional porosity. Beere [22] developed a model, which yields an exponential porosity-dependence. He assumed that [24, 25] (i) pores develop to an equilibrium shape throughout densification (due to e.g. rapid surface diffusion) and (ii) the stress inside the material is virtually hydrostatic. In this model the pores are located at edges of grains with tetrakaidecahedron shape. They have complex curvature and meet the grain boundaries at constant dihedral angle θ satisfying the surface tension balance ($\theta = \arccos(\gamma_{gb}/2\gamma_s)$, where γ_{gb} is the grain boundary surface energy and γ_s is the surface - vapour surface energy). The shapes calculated by Beere correspond to a minimum in free energy of the pores at constant volume. The validity of this model is confined to a certain porosity range, which depends on the dihedral angle. For $\theta = 75°$ this range extends from 55% to 6% porosity. The upper and lower threshold volume are defined by the volume at which, respectively, the contact area is completely consumed by porosity or interconnected porosity can no longer exist. Both threshold volumes decrease with decreasing dihedral angle. In Fig.3 Beere's stress multiplication factor is shown for different dihedral angles (note that θ cannot be larger than 90°). Viera & Brook [26] demonstrated that these curves can be well approximated by:

$$\phi = \exp\{a(\theta)P\} \tag{5}$$

where a(θ) > 0 and a (θ) decreases with increasing dihedral angle. The function a(θ) is, in fact, well described by a second-order polynomial expression:

$$a(\theta) = 13.16 - 0.1657\theta + 0.0007\theta^2 \quad (6)$$

For most oxides θ equals approximately 75°, which gives a = 4.8.

The contact models [21, 27, 28] all assume a random dense packing of monosized spheres as the starting geometry. The continuous increase of the number of contacts per particle, i.e. the coordination number (Z), and the growth of the average contact area are then modeled. To do so, it is imagined that the radius of the particles increases around fixed centres, contacts are represented by truncations of the spheres and the mass removed by truncations is redistributed in the void space, thereby further increasing the neck radii. Again the stress is assumed to be hydrostatic and calculation of the stress per contact area in relation to the applied stress gives the stress multiplication factor. These models are rather complex. Helle *et al.* [28] showed that the exact solutions can be simplified without introducing significant errors considering uncertainties in material's properties and experimental conditions. They obtained a convenient, simple solution for ϕ:

$$\phi = \frac{(1 - \rho_0)}{(\rho^2 (\rho - \rho_0))} = \frac{P_0}{((1 - P)^2 (P - P_0)^2)} \quad (7)$$

where ρ_0 and P_0 are the initial density and initial porosity respectively. In Fig.3 the stress multiplication factor according to Eq.(7) is shown for ρ_0= 0.55 and 0.64. It can be seen that the porosity-dependence of the approximation of Helle *et al.* is even stronger as that of Beere's solutions at low densities. For densities above 70% both models yield fairly comparable values. The contact model is not valid for loose-packed powders ($\rho_0 \leq 0.50$), since large scale particle rearrangement will occur at such low densities either as a result of local variations in coordination number or under the influence of the applied stress [21].

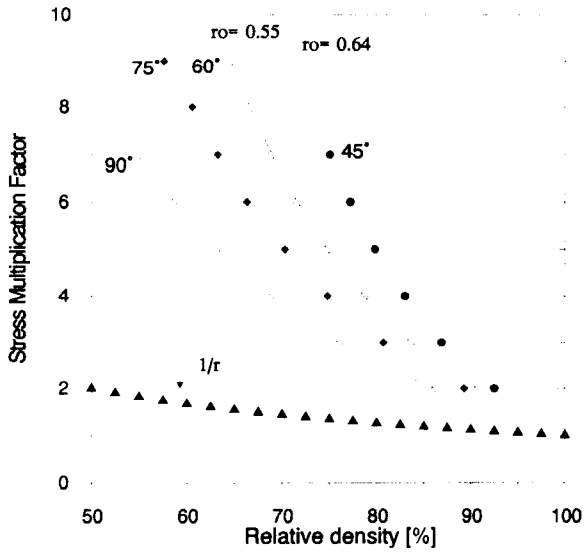

Fig. 3. ϕ as function of relative density using several models; Helle (at different initial densities r_0); Beere (at different dihedral angle in °); Filled triangles: Coble. (Eq .1)

At high densities (above 90%) both type of models break down: Beere's model, as mentioned above, because the porosity is no longer interconnected and the contact models because the contacts become too large to ignore interaction. Moreover, in these models the coordination number Z has a limiting value of 12 at full density, whereas in real, fully dense materials Z equals 14. At high densities the linear porosity-dependence of Eq.(4) proposed by Coble is most appropriate, which gives ϕ-values only slightly larger than 1, as can be seen in Fig. 3.

3.2. Comparison with experiments.

During hot-pressing it has generally been observed that the density increases linearly with the logarithm of time [26]. If the densification rate is grain size dependent, this so-called semi-logarithmic law can be explained by grain growth under certain conditions [29]. However, Viera & Brook [26] also observed this semi-logarithmic relationship (in the density range 0.75 to 0.92) for hot pressing of MgO, densifying by plastic flow. Plastic flow is insensitive to grain size and the interpretation on the basis of grain growth does therefore not apply. In [26] it was demonstrated that these results can be explained by a stress multiplication factor, that depends exponentially on porosity as in Beere's model. Rahaman *et al.* [20] analyzed the sinter forging behaviour of CdO under very low uniaxial stresses (0 - 0.25 MPa) and also found that ϕ has an exponential porosity-dependence. The absolute value was, however, significantly smaller than predicted by Beere's model using the experimentally determined dihedral angle.

An interesting method to directly measure the stress multiplication factor is the study of densification under stress of metal compacts by yielding. Macroscopic yielding starts once the local stress exceeds the stress required for yielding. Due to the constrained nature of the contacts the yield stress (σ_y) is generally assumed to be three times the flow stress for unconstrained deformation. The ratio $3\sigma_y/\sigma_a$ (σ_a is the applied stress) is thus equal to ϕ and can be analyzed for different densities. This analysis gives an exponential dependence of ϕ for different metals over a large density range [21]. The functional form predicted by Beere is observed in this way, but the experimental value is larger than predicted in this case (assuming θ equals 80°), since for most metals the grain boundary energy is one third of the surface energy [30]. As shown by Funkenbush *et al.* [21], contact models for ϕ are in essential agreement with these experimental data over a limited density range (70 - 85%). At lower densities the predictions are much too large.

In conclusion, one can say that Beere's model correctly describes the functional form of ϕ, but the constant a should rather be used as an adjustable parameter, which must be determined experimentally. If no equilibrium pore morphology is developed, Beere's model cannot be used and the contact models should be preferred. Both models can be considered as complimentary: each is most applicable under conditions where the other is least [21].

4. Constitutive equations governing creep and densification

As mentioned in section 2, both densification and macroscopic creep occur during sinter forging. From our experiments performed on TZP ceramics [18], it has become clear that creep governs densification during sinter forging. However, at present, detailed models are not available for sinter forging, which relate both processes and predict the densification rate, like those developed by Coble [23] for hot pressing and Ashby and co-workers [28, 31] for hot isostatic pressing. For hot pressing and hot isostatic pressing, the coupling between creep and densification is often performed in a rather straightforward way, which will now be briefly described.

High temperature deformation of dense materials can be described by the well-known phenomenological flow law:

$$\dot{\epsilon} = \frac{AD}{kT}\frac{\sigma^n}{G^p} \tag{8}$$

where $\dot{\varepsilon}$ is strain rate, A a numerical constant, D the diffusion coefficient, k Boltzmann's constant, T temperature, σ the applied stress, n the stress exponent, G grain size and p the grain size exponent. The creep parameters n and p generally have values between 1 and 3 for ceramics. For hot pressing

the densification rate is related to the axial strain rate by:

$$\dot{\epsilon}_v = -\frac{1}{\rho}\frac{d\rho}{dt} = -\dot{\epsilon}_z \tag{9}$$

whereas for HIPing the following relationship holds:

$$\dot{\epsilon}_v = -\frac{1}{\rho}\frac{d\rho}{dt} = -3\dot{\epsilon}_z \tag{10}$$

Roughly, one can now obtain the relationship between creep and densification for these pressure sintering methods by incorporating Eq.(8) into either Eq.(9) or Eq.(10), after replacing σ by the effective stress for a porous material.

A relationship, similar to Eq.(9) or Eq.(10), between densification and axial strain rate does not exist for sinter forging (see Eq.(1), section 2). It is reasonable to assume that the driving force for densification and creep are respectively, the hydrostatic stress (p) and the deviatoric stress (σ_e). Neglecting the sintering stress, the hydrostatic stress equals ($\sigma_z/3$) and the deviatoric stress is equal to the absolute value of σ_z [16]. The creep rate can then be written in a way similar to Eq.(8):

$$\dot{\epsilon}_c = \frac{2}{3}|\dot{\epsilon}_z - \dot{\epsilon}_r| = \frac{AD}{kT}\frac{(\phi\sigma_e)^n}{G^p} = \frac{AD}{kT}\frac{(\phi|\sigma_z|)^n}{G^p} \tag{11}$$

Constitutive equations for densification during sinter forging can be obtained from the models derived for hot isostatic pressing by several mechanisms [28, 31], as will now be shown in detail for grain boundary diffusion controlled sintering.

The sintering process is generally divided into three stages: (1) the initial stage, where discrete particles join together by neck growth and total shrinkage is limited to a few per cent, (2) the intermediate stage, where a continuous pore channel has developed, pores are essentially cylindrical and the largest part of shrinkage occurs and (3) the final stage, where pores becomes isolated and can be viewed as spheres. Models for HIPing are likewise divided into these stages, due to the differences in pore geometry. During heating to the temperature used for pressure assisted sintering, some densification usually occurs and the material is often already in the intermediate stage before the stress is applied. Therefore, only the last two stages of sintering are of interest in modelling pressure assisted sintering. The final stage is generally considered to start once the density has become more than 90%. As described in section 3, different expressions have to be used for the stress multiplication factor above and below 90% relative density.

The development of a constitutive equation for the densification rate during sinter forging from HIPing models, will now be illustrated for grain boundary diffusion control. Helle *et al.* [28] have developed simplified expressions for this case from the more complex, exact solutions [32]. For the intermediate stage they obtained the following expressions:

$$\frac{d\rho}{dt} = \frac{43(1-\rho_0)^2}{(\rho-\rho_0)^2}\frac{D_{eff}\,\Omega}{kTR^3}p \tag{12}$$

with R the particle radius and D_{eff} the effective diffusion coefficient for this stage, all other symbols having their previously defined meaning. In deriving Eq.(12), Helle *et al.* used Eq.(7) for the stress

multiplication factor. The effective diffusion coefficient is given by:

$$D_{eff} = \partial D_{gb} + R(\rho - \rho_0) D_l \tag{13}$$

where δ is the grain boundary thickness, D_{gb} is the grain boundary diffusion coefficient and D_l is the lattice diffusion coefficient. The hydrostatic stress during sinter forging is:

$$p = \frac{\sigma_z}{3} \tag{14}$$

so the equation for the densification rate in the intermediate stage of sinter forging becomes:

$$\frac{d\rho}{dt} = -\frac{43(1-\rho_0)^2}{3(\rho-\rho_0)^2} \frac{D_{eff}\,\Omega}{kTR^3} \sigma_z \tag{15}$$

The equation for the final stage, as developed in the same way from the final stage model of Helle *et al.*, is:

$$D'_{eff} = \partial D_{gb} + R\left(\frac{1-\rho}{6}\right) D_l \tag{16}$$

The effective diffusion coefficient D'_{eff} in this stage is given by:

$$\frac{d\rho}{dt} = \frac{90\sqrt{(1-\rho)}\, D'_{eff}\,\Omega}{kTR^3} \sigma_z$$

For final stage HIPing, Helle *et al.* assumed the effective pressure to be identical to the applied pressure (which is reasonable, considering Eq.(4) for ϕ in this density range). Kwon *et al.* [33] have shown that the sinter forging kinetics of alumina can be well described in this way, if one takes dynamic grain growth into account. It is obvious, that this analysis can only be performed, if the relevant diffusion coefficients and grain growth kinetics are known.

If the observed stress dependence of the densification rate is larger than 1, as observed for TZP ceramics (see section 6), it would be more appropriate to develop equations for densification from the model, given by Wilkinson & Ashby [31], for HIPing by power law creep.

5. Defect elimination during sinter forging

In the preceding section, constitutive equations have been given for densification during sinter forging, based on HIPing models. In these models, pores are assumed to be situated at three-grain-edges or four-grain corners in respectively the intermediate and final stage of sintering. The pore size is thus related to and smaller than the average grain size G. In well-packed compacts, the vast

majority of pores is indeed smaller than the average grain size and the evolution of their volume with time gives the sintering behaviour. However, inevitably in ceramics, some pores are present with sizes much larger than G and these pores or flaws are strength controlling in the sintered product. Continuum models are needed to understand the behaviour of these flaws during sinter forging. Budiansky *et al.* [9] have analyzed the deformation of voids under axisymmetric loading in linearly and nonlinearly viscous materials.

In the case of a Newtonian viscous material (i.e. the stress exponent n = 1), an analytical expression could be obtained for the change in aspect ratio, λ, of an ellipsoidal void with axial strain ε. For uniaxial compression, this expression is independent of the applied stress:

$$\frac{d\lambda}{d\epsilon} = \frac{3\lambda^3(2-\beta)}{2\alpha(2\lambda^2+\beta(1-\lambda^2))} = f(\lambda) \tag{17}$$

where:

$$\beta = \frac{\lambda}{(1-\lambda^2)^{3/2}}[\arccos(\lambda)-\lambda\sqrt{(1-\lambda^2)}] \tag{17a}$$

and

$$\alpha = \frac{\lambda^2(3\beta-2)}{(\lambda^2-1)} \tag{17b}$$

The aspect ratio (λ) is defined as the ratio of height and diameter of the ellipsoidal void. We will limit our discussion to oblate ellipsoids ($\lambda \leq 1$). If one would plot α versus λ between 0 and 1, several interesting features can be seen. Firstly, $f(\lambda)$ (= α) equals zero both for $\lambda = 0$ (physically not meaningful) and $\lambda = 1$. A perfectly spherical void will thus not change its shape during compression. Between 0 and 1, $f(\lambda)$ increases in a almost linear fashion (from approximately 1 to 2.5). It can be shown that it follows from this that the aspect ratio will decrease exponentially with strain.

The strain required to close a pore (ε_{cl}) can be obtained from numerical integration of Eq.(18):

$$\varepsilon_{cl} = \int_{\lambda_0}^{0} \frac{d\lambda}{f(\lambda)} \tag{18}$$

where λ_0 is the initial aspect ratio. The results of this integration are shown in Fig. 4. It can be seen that the closure strain increases with the initial aspect ratio. For instance, for $\lambda_0 = 0.2$ the closure strain equals -0.18 and increases to -0.62 for a spherical void ($\lambda_0 = 1$). It should be borne in mind that the model of Budiansky *et al.* applies to an incompressible solid. To apply it to a sinter forging material, one should take the creep strain as the appropriate strain parameter (Eq.(1)).

No analytical expression equivalent to Eq.(17) could be derived for a nonlinearly viscous material (n > 1). However, it can be seen from the results in [9], that the dilatation rate of voids is not very sensitive to the value of the stress exponent for uniaxial compression. Therefore, Eqs. (17) & (18)

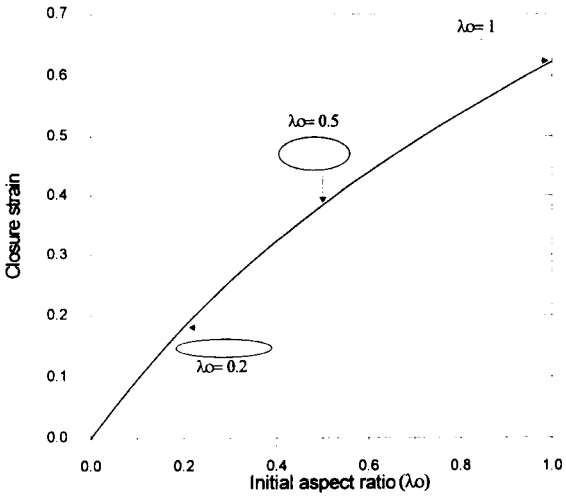

Fig. 4. Strain requried to close a pore as function of the initial aspect ratio (after [5]).

should also serve as a reliable guideline for non-Newtonian materials, especially if one considers the limited variation of n in ceramics (n = 1 - 3).

Some evidence has been found for the validity of the continuum model of Budiansky *et al.*. Venkatachari & Raj [5] found that the strength of sinter forged alumina increases sigmoidal with increasing creep strain until it saturates at a strain near 0.6. These authors found that this strength-increase correlates with the gradual disappearance of flaws with creep strain. Since alumina deforms by a Newtonian mechanism, Fig. 4 applies to this material and is confirmed by the data of Venkatachari & Raj [5]. Kellett & Lange [8] analyzed pore closure during hot forging of zirconia dispersed alumina, containing pores, which were remnants of monosized plastic spheres. Pores, located near the edge of the specimens (where the influence of friction is negligible), disappeared completely at an engineering strain of -0.6. Pores located within the so-called friction hill, where triaxial compression occurs, disappeared at smaller engineering strains. In the model of Budiansky *et al.*, however, strain is defined logarithmical and the closure strain in [8] thus equals -0.9. Zirconia dispersed alumina deforms by a non-Newtonian mechanism (n = 2) and the closure strain thus seems to increase with increasing stress exponent.

This is corroborated by the data of Panda *et al.* [6], who found that powder compacts of Y-TZP, creeping by a non-Newtonian mechanism, require a critical amount of compressive strain to consolidate to full density during sinter forging at 1400°C, independent of stress and strain rate. Their observed value for the closure strain (-0.95) agrees almost exactly with the one in the analysis of Kellett & Lange. This indicates that densification was controlled by removal of pores larger than the grain size, for which the model of Budiansky applies. Such a situation can arise, when a compact consists of a packing of agglomerates of very fine crystallites. Such agglomerates can already densify completely during heating and any further densification will be controlled by the remaining large, interagglomerate pores. Unfortunately, Panda *et al.* did not analyze the microstructure before the start of compression. These authors observed a stress exponent n = 3 and interpreted their data in terms of grain-size insensitive dislocation creep. However, at present, abundant evidence is available showing that creep of very pure TZP is characterized by n = 3 under particular thermomechanical conditions, but is not related to dislocation creep.

6. Sinter forging kinetics

The sinter forging behaviour of tetragonal zirconia (TZP) will be treated by means of the results fully described in [18]. In this paper the TZP systems stabilized with Y_2O_3 and Y_2O_3 plus CeO_2 are discussed. The sinter-forging mechanisms and the processing paths of both systems are identical. Therefore only the results on Y_2O_3 doped nanocrystalline (crystallite size 8 nm) TZP (Y-TZP) will be given here. The sinter-forging tests were performed in air at several constant loads at a temperature of 1100°C. Prior to sinter forging a presintering step at 950°C was incorporated resulting in stronger samples (due to neck formation) with only a slight increase in density (from 45%

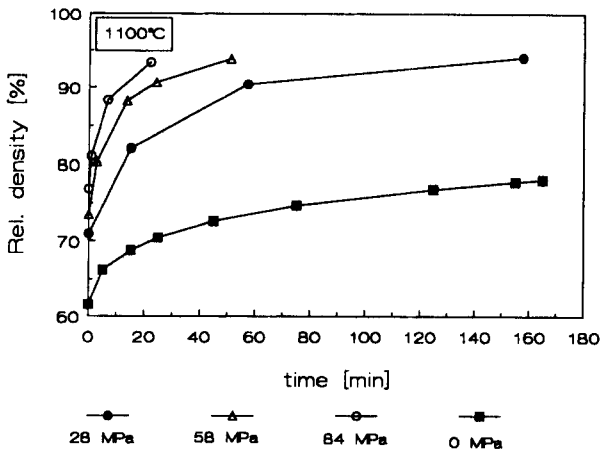

Fig. 5. Increase in relative density as function of time druing free sintering (0 MPa) and sinter forging.

Table 1 Sinter behaviour of Y-TZP at 1100°C as function of applied load

Initial load (MPa)	time (min)	rel. density (%)	grain size (μm)
0	900	92	0.18
28	160	94	0.13
58	50	94	
84	22	94	0.10

to 49%) [18]. During heating up to the test temperature also densification occurs. This results in a radial and axial shrinkage. Because the strains are defined with respect to the dimensions prior to the sinter-forging test, a negative value of the radial strain is registered at the moment compression starts at 1100°C (see Fig.6).

The increase in relative density with time during free sintering and sinter forging under initial stresses of 28, 58 or 84 MPa at 1100°C is shown in Fig. 5. All compacts are from the same (nanocrystalline) powder batch [18]. Green densities and pore morphology of the green and presintered compact are in all cases identical. For free sintering 900 minutes were necessary for obtaining a 92% dense ceramic. Sinter forging under 84 MPa pressure requires less than 30 minutes to reach a relative density of 94% at the same temperature. So clearly a strong reduction in sintering time is observed. In Table 1 final densities minimal sintering times and resulting grain sizes are given.

In Fig. 6 the processing paths ε_r versus ε_z of these experiments are shown. The variation in diameter is only very small under an initial stress of 28 MPa so here contraction, due to sintering, is balancing with expansion due to creep. Because the load was kept constant during this experiment, the actual stress decreases for the samples sinter forged at initial stresses of 58 and 85 MPa. At achieving the final density of 94% after resp. 50 and 22 minutes actual stresses of 52 and 73 MPa are observed for the 58 and 84 MPa sinter-forged samples [34]. The processing paths of these two samples are high strain paths as indicated in Fig. 1.

The stress dependence of the creep strain rate during forging has been analyzed assuming the relation $\dot{\varepsilon}_c \sim \sigma_e^n$ holds, where n is the creep stress exponent. In Fig. 7 this stress dependence of the creep strain rate is shown for Y-TZP with a grain size of 0.1 μm and relative densities of 85, 90 and 98%. [35]. By taking the strain rates at constant density it can be assumed that the stress multiplication factor ϕ is constant. From this figure it can be seen that porosity results in an enhancement of the overall creep strain rate. The stress exponents in these three cases are almost identical (n ~ 2). These n-values are the same during creep of dense (98%) Y-TZP with grain sizes down to 200 nm [36]. Creep behaviour and creep mechanism of these sinter-forged Y-TZP material

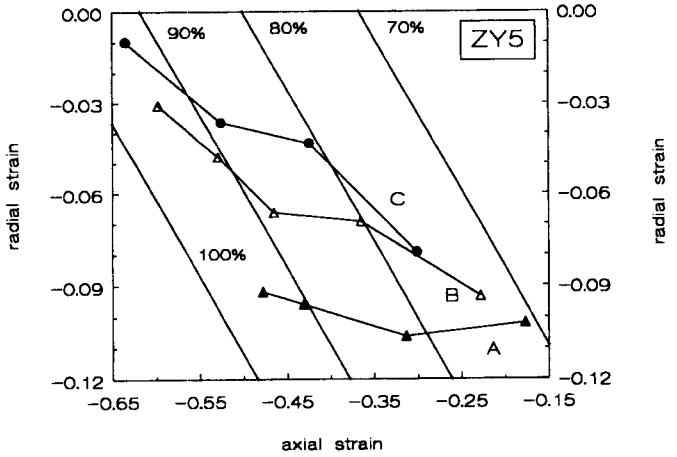

Fig. 6. Processing paths ε_r versus ε_c for Y-TZP sinter forged at 1100°C
A: 28 MPa; B: 58 MPa; C: 84 MPa.

can therefore be compared with the results form creep tests on a dense (>97%) Y-TZP material. The creep behaviour of the dense Y-TZP system has been interpreted as interface reaction controlled grain-boundary sliding, which is in good agreement with the deformation map proposed by Nauer and Carry [37].

In [18] it is shown that nanostructured (grain size 0.1 μm) Y-TZP (and also Y,Ce-TZP) with high relative densities (90-93%) could be obtained by sinter forging of nanocrystalline powders. At this temperature (1100°C) prolonged sinter forging did not increase the density above 94% indicating that at that stage pure creep occurs at constant porosity. Near theoretical (>97%) densities could be obtained with the investigated TZP's by sinter forging during 25 minutes at 1150°C under an initial stress of 80 MPa with a final mean grain size of 0.2μm [18].

From our results and those of other researchers it has became clear that sinter forging is a very suitable pressure sintering technique to prepare dense nanostructured materials. The sinter-forging temperature can further be reduced to 1050°C by using a hydrothermally crystallized powder. Under critical stresses of 75 - 85 MPa densities of more than 95% can be achieved with final grain sizes in the range of 80 - 100 nm. Skandan et al. [2] demonstrated that fully dense nanostructured ZrO_2 can be produced by sinter forging at 950°C at very high stresses (> 200 MPa). These authors used an inert gas condensation technique for powder synthesis while the powders used in our work were prepared by a gel-precipitation technique [18].

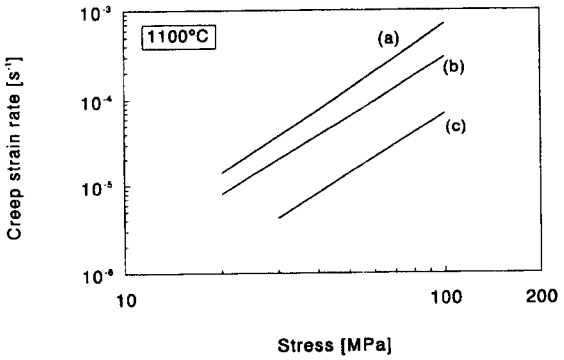

Fig. 7. Stress versus strain rate for Y-TZP at 1100°C with various densities. (grain size 0.1μm) a) 85%, b) 90%, c) 98%.

In these Y(Ce)-TZP no dynamic grain growth is observed [18]. Skandan et al. [2] mentioned a slight increase in grain size from 35 to 45 nm when the forging conditions for Y-TZP varied from 0 to 300 MPa. It should be noted that in this latter case also a slight increase in density was observed with increasing stress. It can be concluded that, if present, only very little grain growth occurs due to increasing applied stress even when using the extreme high value of 300 MPa (Boutz, unpublished work).

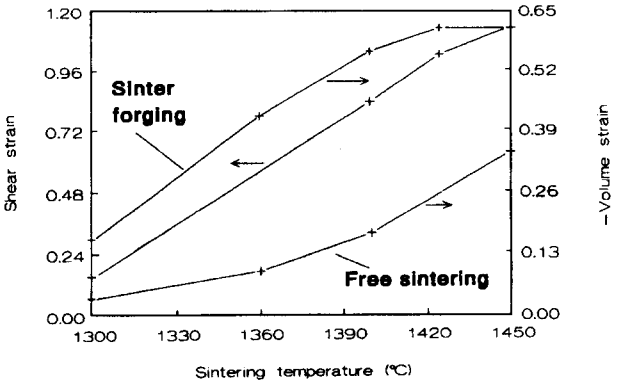

Fig. 8. Volume strain during free sintering and sinter forging and shear strain during sinter forging of ZTA (initial stress 40 MPa)

Sinter forging can especially be interesting for composites if differential sintering of the phases has a detrimental effect on overall densification. As an example sinter forging of 15 wt% (undoped) zirconia dispersed in alumina will be described (ZTA = Zirconia Toughened Alumina) [36]. In Fig. 8 creep (shear) strain, ε_c, and volume strain, ε_v, as function of temperature are given during sinter forging and compared with free sintered ZTA while heating to 1450°C at 2.5°C/min. The applied stress during sinter forging was linearly increased to 40 MPa in the temperature range of 1150 - 1200°C. In these systems sinter forging has a strong beneficial effect on densification too while large creep strains (with a true strain of more than 1.0) are reached just by heating to 1450°C. A dense (98+%) ZTA is obtained after sinter forging for 15 minutes at 1400°C, while at least a temperature treatment of 1450°C for several hours is necessary for obtaining the same density by means of free sintering [35]. A reduction of the sintering temperature by 200°C from 1500°C to 1300°C is observed by sinter forging a 20 vol% ZrO_2 dispersed Al_2O_3 reaction bonded composite [19]. In general one can state that in composite materials a larger reduction in sintering temperature is observed by sinter forging if compared to the monolithic TZP systems. This larger reduction is probably related to the relaxation of differential sintering stresses by creep of the matrix during sinter forging.

After sinter forging no textural development, such as preferential orientation due to anisotropic grain growth or intragranular creep was observed in the system described in Fig. 8. In order to prove this the microstructure was investigated, both parallel and perpendicular to the direction of the applied stress [38]. SEM pictures of both sections were identical. Kellet and Lange [39] however observed a flattening of Al_2O_3 grains perpendicular to the stress axis during deformation of ZrO_2-Al_2O_3 composite materials. This difference in results can be ascribed to the difference in impurity level and the higher temperature (1500°C) used in [39]. Possibly, dislocation creep contributed to the total deformation at this high temperature. It is also argued that a homogeneous distribution of the zirconia grains at multiple grain junctions of the alumina matrix suppresses grain growth of alumina to an elongated particle morphology [38, 39].

7. Pore morphology development during sinter forging

Sinter forging can result in a rearrangement of the grains in the intermediate and in the final densification stage. Therefore also the pore morphology is influenced by this sintering technique. Pore coarsening as well as pore fragmentation into smaller pores can occur. In this section first some

examples will be given on pore morphology evolution during the intermediate sintering stage, while finally some remarks are given about the final (pore closure) stage.

The evolution of the pore size distribution during free sintering and sinter forging (initial applied stress 28 - 84 MPa) of Y-TZP in the intermediate stage is described in [35]. All samples had the same density (80% rel.) and an identical grain size of 40 nm. A very broad pore size distribution is observed in the free sintered material. After sinter forging the volume of pores with radii 15 - 17 nm increases strongly, while small pores (radius < 10 nm) disappear progressively at increasing stress. This means that the pore size to grain size ratio is more uniform resulting in more homogeneous densification of the compact. In the free-sintered compact this ratio is strongly varying over the compact giving inhomogeneous densification and consequently local differential stresses inhibiting further local densification and (micro) crack formation. A possible mechanism for the smaller pores to disappear during sinter forging is the coalescence to larger pores. This reorganisation to a more homogeneous compact is a better start for final sintering stage in order to obtain a dense fine-grained ceramic with a homogeneous microstructure.

Another example of a change in pore morphology during the intermediate sintering stage by means of sinter forging is shown in Fig. 9 for ZTA. In this experiment alumina in the starting ZTA powder compact has a transition alumina crystal structure (θ-phase) [40]. Here the phase transformation from θ to α-Al_2O_3 at around 1250°C is an extra phenomenon in the intermediate sintering stage. During this phase transformation a rearrangement of the pore morphology occurs [40]. In Fig. 9 the pore-size distribution is given after sintering at a temperature where after the θ → α-Al_2O_3 transformation just has occurred (1250°C). A slight increase in pore size is observed when the sample is sinter forged. The main difference between sinter forging and free sintering is the presence of the broad tail of small pores in the free-sintered compact. These small pores in the free-sintered samples are remainders of intra-aggregate pores of the porous θ-alumina aggregates. After the θ - α phase transformation the free-sintered compact consists of irregularly shaped α-Al_2O_3 crystallites with irregularly shaped pores [40]. The external pressure during sinter forging results in shear deformation which densifies the theta alumina aggregates and/or results in an internal reorganisation during the θ to α-Al_2O_3 phase transformation. This provides the opportunity to eliminate the small intra-aggregate pores and transform them to larger inter-aggregate pores resulting in a more homogeneous microstructure for further densification [38]. Applying a stress while sinter forging the transition alumina (θ-Al_2O_3) matrix is here of prime importance for sinter forging these ZTA systems to full density at relatively low temperatures (1400°C).

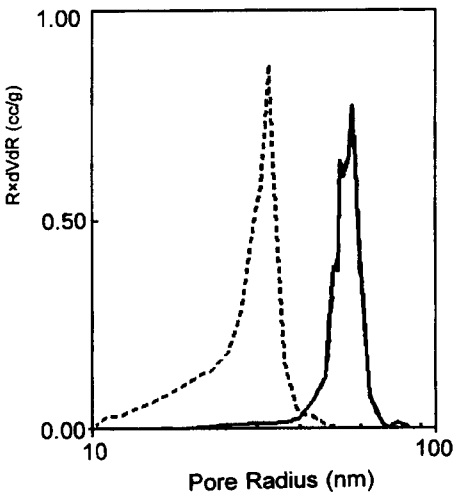

Fig. 9. Pore size distribution (on a log scale) of a ZTA compact after phase transformation to α-Al_2O_3 (1250°C).
dotted line: free sintered
solid line: sinter forged

Mayo et al. [41] observed for nanocrystalline TiO_2 the removal of large pores if sinter forging was applied. Here they studied powders whose agglomerates could not be eliminated during synthesis. At a stress of 60 MPa a preferential closure of large inter agglomerate pores was observed resulting in a nearly perfect microstructure for densification these TiO_2 at a temperature as low as 610°C.

From the discussion given above it can be concluded that high creep strains are important for

a rearrangement to a more homogeneous microstructure in the initial or intermediate sintering stage, where open porosity is present. In all cases the ratios of grain (crystallite) sizes to pore sizes become more uniform by sinter forging. In this way the number of grains around a pore (the pore coordination number) becomes more uniform while its value reduces to a sufficient low number in order to obtain a uniform compact for full densification.

Sinter forging can also strongly influence the final sintering stage. The stage where pore shrinkage and pore closure occurs. Venkatachari and Raj [4] observed in alumina by SEM that in this sintering stage pores with sizes exceeding the mean grain size ("flaws") are flattened and fragmented into smaller ones and gradually disappear with increasing strain during sinter forging. Panda et.al [6] suggested that pore closure during sinter-forging of Y-TZP occurs by plastic flow, which means that the densification rate is related only to the applied plastic strain (see also section 5 of this chapter).

It is however also possible that during sinter forging to large strains cavitation occurs by non-accommodated grain-boundary sliding resulting in new small pores [41]. In this way a steady state equilibrium can be established between density loss due to cavitation and density increase due to (diffusional) pressure sintering and no further increase in density will occur during prolonged sinter forging. This can especially occur when creep strains (and consequently applied stresses) are too large. In generally it can be concluded that sinter forging can be used to selectively close deleterious pores if sinter forging is performed in an appropriate deformation regime.

8. Mechanical properties of sinter-forged systems

Sinter forging if applied correctly results in a more dense ceramic with smaller and less processing flaws (cracks) as can be concluded from the results and the theoretical considerations given in this chapter. If this is the case the mechanical properties will be improved. Strength, toughness and the mechanical property related wear resistance will be discussed now.

The fracture toughness (K_{IC}) and bending strength (σ) values given here are obtained by single edge notched beam and 4 point bending tests respectively. Also some hardness values are measured by micro (Vickers) indentation From the measured K_{IC} value the fracture surface energy at zero porosity γ_0 is calculated by means of:

$$\gamma_f = \gamma_o \exp(-bP) \tag{19}$$

b is a numerical constant, found to be 3.4 by Boutz et al. [42] and P the residual porosity. The fracture surface energy, γ_f, necessary to create a unit area of new fracture surface, is directly related to K_{IC} at plane stress conditions by:

$$\gamma_f = \frac{K_{IC}^2}{2E} \tag{20}$$

where E is Young's modulus.

The bending strength data are assumed to follow the Weibull probability function. In Weibull statistics, the cumulative probability function, $P(\sigma)$, the probability of failure at or below a stress σ, is given by [43]

$$P(\sigma) = 1 - \exp[-(\sigma/\sigma_0)^m] \tag{21}$$

where m is the Weibull modulus and σ_0 is a scale parameter with the same dimension as σ. The Weibull modulus is a measure for the reliability of a ceramic in engineering applications.

In Table 2 some mechanical data are given of Y-TZP with a grain size of 0.2 μm. This microstructure was obtained after free sintering for 10 hours at 1150°C or after sinter forging for

Table 2: Mechanical properties of free and sinter-forged Y-TZP [44, 45]

	Hardness H_V (GPa)	K_{IC} (MPa$\sqrt{m}$)	γ_0 (J/m^2)	Weibull mod. m
Free sintered	13	8	210	8
Sinter forged	14	10	300	21

25 minutes at 1150°C at an initial stress of 80 MPa starting in both cases with an identical, nanocrystalline, weakly agglomerated powder (crystallite size 8 nm) [18, 34].

The fracture toughness of this Y-TZP system increases after sinter forging from 8 to 10 MPa$\sqrt{m}$. The crystal structure of the ceramic bulk as well as the fractured surface of these TZP's was found to be 100 % tetragonal. The toughening mechanism can therefore not be ascribed to an (irreversible) stress-induced phase transformation of tetragonal to monoclinic zirconia. The free-sintered as well as the sinter-forged sample fracture intergranularly. In combination with the higher fracture surface energy this is an indication that the higher toughness for the sinter-forged samples is caused by an improved (stronger) grain-boundary morphology with less microdefects [45]. This will be further discussed in section 10.

The fact that sinter forging has a beneficial effect on reliability is best demonstrated by the increase in Weibull modulus (m) from 8 (free sintered) to 21 (sinter forged) as calculated from 10 measurements [45]. Since strength and reliability are sensitive to the presence of flaws it is clear that in this Y-TZP system the flaw size and especially the concentration of large flaws is drastically reduced by sinter forging.

In Table 3 the mechanical properties are given for ZTA after free sintering (2 hours) and sinter forging (15 min. 40 MPa) at 1450°C. Both systems had a relative density of 98% and a zirconia and alumina grain size of respectively 0.3 and 0.8 μm. After sinter forging the total creep strain was more than 1.0 (see also Fig. 8).

These results show an increase in (4-point) bending strength by a factor 2 if sinter-forging is applied while both samples had a relative density of 98% (the relative low strength values, if compared with literature, are probably caused by cracks at the sharp edges of the samples which arose during machining and were not removed prior to mechanical testing). For 20 vol% ZrO_2 dispersed reaction bonded alumina Boutz et al. [19] measured a biaxial bending strength of 1115 MPa after sinter forging, whereas after free sintering strength equals only 400 - 600 MPa. These increases in strength indicates that flaws are effectively removed by the large creep strains [46].

The fracture toughness increases 50% (table 3) by sinter-forging. XRD analysis showed that most of the zirconia particles in the bulk ZTA ceramic are in the tetragonal form, while after fracture 30 vol % of the zirconia at the fractured surface is transformed to monoclinic zirconia [46]. The amount of transformed zirconia is not influenced by sinter forging. So the contribution of stress induced phase transformation as toughening mechanism is the same for both systems.

Table 3: Mechanical properties of free and sinter-forged ZTA [46]

	Strength σ_f (MPa)	K_{IC} (MPa$\sqrt{m}$)	γ_0 (J/m^2)
Free sintered	380	5.2	38
Sinter forged	800	7.4	73

The difference in mechanical properties and identical transformation behaviour indicate that for the sinter-forged samples an extra toughening mechanism occur. All samples fracture intergranularly so the difference in mechanical properties can be ascribed to an improved grain-boundary morphology by sinter forging.

In [16] it is shown for alumina that the strength increases with creep strain which is also discussed in section 5 of this chapter (see Fig. 4). It is suggested in [16] that sinter forging can completely remove internal processing flaws and consequently increase strength and reliability as is also shown by the results given in this section.

The results given in this section indicate that sinter forging of composites gives a stronger improvement on mechanical properties if compared to monolithic TZP systems. This phenomenon is in agreement with the improved densification behaviour as discussed in section 6.

9. Tribological properties

The influence of sinter-forging on friction and wear behaviour of two ZrO_2-Al_2O_3 composite materials are described in [47]. One system was ZTA, while TZP was the main phase in the other composite (20 wt.% Al_2O_3 dispersed in a Y-TZP matrix = ADZ). Sliding wear tests were carried out using a SiC ball-on-plate tribometer where the ball slides reciprocally on the plate under a normal load of 8 N corresponding to a Hertzian contact pressure of 858 MPa [44, 47]. A measure for the wear resistance is the wear rate K which is the wear volume loss normalised to the wear track length and the applied normal load (K in mm^3/Nm).

In Table 4 the wear rate is given of both composites with and without sinter forging. Within each set of composites (ZTA or ADZ) density and grain size are identical. So an observed difference in wear properties can be ascribed to the influence of sinter forging. From the results it can be seen that sinter forging of ZTA has a beneficial effect on the wear resistance. A decrease in wear rate by a factor 2-3 is observed in this case while the amount of monoclinic zirconia on unworn and worn surfaces (resp. V_b and V_{worn}) are independent of the sintering method. On the other hand sinter forging has no influence on the wear resistance of the ADZ composite (remark however the very low wear rate of ADZ, also compared with single phase Y-TZP as measured in the same tribometer [44]). This difference in influence of sinter forging on K can be explained by considering the several wear mechanisms.

Scanning electron microscopy observations of worn surfaces indicate that polishing and grain pull-out are the main wear mechanisms in ZTA ceramics [43]. At the turning points of a wear track of free-sintered ZTA also microcracks were observed. In the sinter-forged specimens no microcracking or scaling patterns were present. Examination of the wear tracks indicates almost the same wear mechanism as for free-sintered ZTA. Grain pull out is however less pronounced in the latter case.

Table 4. Sliding wear properties of a SiC ball on ZrO_2-Al_2O_3 ceramic plates [44, 47].

Sample code	Grain size (μm)		wear rate $K\times10^{-6}$	perc. monoclinic ZrO_2	
	ZrO_2	Al_2O_3	[mm^3/Nm]	V_b	V_{worn} (vol%)
ZTA - sinter forged	0.3	0.8	1.44 ± 0.31	5	15
ZTA - free sintered	0.3	0.8	3.40 ± 0.90	6	14
ADZ - sinter forged	0.3	0.4	0.43 ± 0.04	0	0
ADZ - free sintered	0.3	0.4	0.40 ± 0.02	0	0

The energy necessary for grain pull-out is related to the fracture surface energy (γ_0) if the material fractures intergranularly as is the case for these systems (see section 8). Grain pull-out requires more energy if the bonding strength between the grains increases. So an increase in γ_0 by sinter forging (which can be related to an increase in grain-boundary strength), also gives a decrease in wear rate if grain pull-out is one of the main wear mechanisms.

During a fatigue wear process, as is obviously the case at the turning points of the ZTA systems, micro defects can easily grow to local flaws or cracks. A source of such micro defects are large inter-atomic spacings, which are easily formed between grains during sintering (see section 10; Fig. 10). The wear results indicate that micro cracks are effectively removed by sinter forging.

Under the present testing conditions, a mild wear occurs in both ADZ materials. The worn surfaces are very smooth with only a very little amount of grain pull-out with absence of any microfracture [44, 47]. For these tribological systems the bonding strength between grain boundaries has no influence on the wear rate. So dependent on the wear mechanism sinter forging can have a beneficial influence on wear rate.

10. Grain boundary morphology

The creep behaviour of ultra-fine TZP materials during sinter forging, especially in the final sintering stage, has been interpreted as interface reaction-controlled or grain boundary diffusion-controlled grain boundary sliding [18]. Sinter forging not only eliminates flaws, but also changes grain boundary morphologies. Grain boundary regions are often characterised by imperfect contact between grains and by segregation of impurities. In order to demonstrate the possible change of the grain-boundary morphology by sinter forging, the hard sphere description of Gleiter et al. [48, 49] for nanocrystalline materials is adopted. In this description the materials consist of two phases: a crystalline bulk-component formed by regular lattice atoms and an interfacial (grain boundary) component containing all atoms which are situated in grain boundaries.

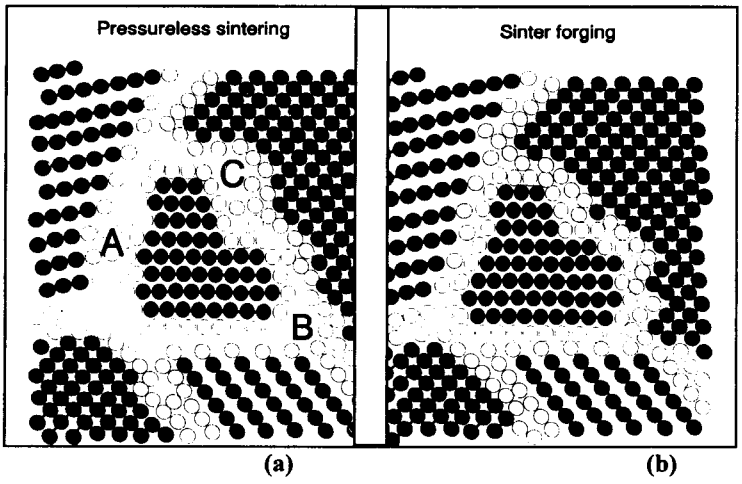

Fig. 10: Schematic representation of an ultra fine-grained ceramic distinguishing between the atoms associated with the individual crystals (solid circles) and those constituting the grain boundary network (open circles). The boundary atoms are shown in regular lattice positions, but in reality will relax to form different atomic arrangements (based on the model in Refs. [48, 49]).

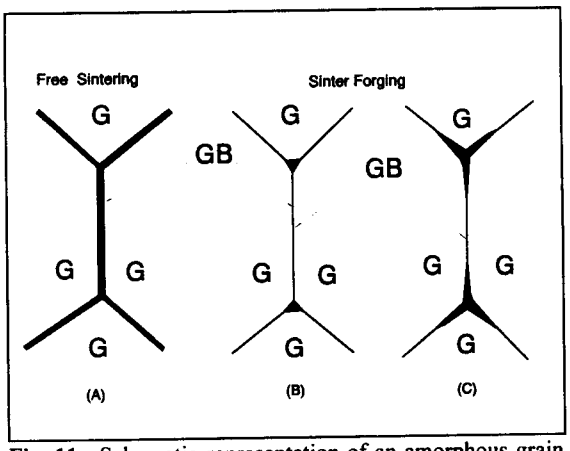

Fig. 11. Schematic representation of an amorphous grain boundary after free sintering (A) and sinter forging (B,C).

A simple two-dimensional picture is given in Fig. 10. The grain boundary if compared with the grain bulk exhibits a different solid state structure with a more random atomic arrangement (A in Fig. 10a) or consists of places where certain interatomic spacings are not filled completely due to incoherence between adjacent crystal lattices [49], e.g., the local areas B and C in Fig. 10a. For ceramics obtained by free sintering large interatomic spacings can be formed at the grain boundaries and result in a relative thick grain boundary layer with a large concentration of micro-defects. Another schematic representation of a grain boundary is given in Fig. 11. If the ceramic has a relative high impurity level an amorphous phase can be present as a film around the grain boundary. (Fig 11A).

During sinter forging the creep deformation results in a rearrangement of the grain boundaries. Some impurities which are segregated to the grain boundaries are moved to grain-boundary junctions. The low energy traps are gradually filled and interatomic spacings are reduced. This process results in a thinner and more regular grain boundary layer (see Fig. 10b) or in a discontinuous amorphous films (see Fig. 11B and C). The change in grain-boundary morphology by sinter forging into a more "improved" grain-boundary morphology can be explained by using the models as illustrated in these figures. This improvement in morphology will now be discussed for the effect of sinter forging on mechanical and tribological properties.

Krell and Blank [50] introduced a microscopic grain boundary energy (Γ^{gb}) and a microscopic grain boundary toughness K_{IC}^{gb} in order to understand the mechanism of fracture toughness and strength enhancement by improving grain boundary structures. They have found that an increased volume of amorphous grain-boundary phase and an increment in grain boundary microporosity are often accompanied by a decrease in grain boundary toughness. The improvement of grain-boundary morphology by sinter forging can result in the enhancement of the microscopic K_{IC}^{gb} and can therefore raise both the macroscopic toughness at crack instability and the resistance against subcritical crack growth. So grain boundaries, strengthened by sinter forging provide a higher resistance to crack propagation and a higher fracture energy, resulting in an increase in grain boundary toughness (K_{IC}^{gb}). As indicated by Krell et al. [50], a higher grain boundary toughness (K_{IC}^{gb}) gives a higher macroscopic toughness.

The strengthening of grain boundaries and/or the removal of microflaws by sinter forging ZTA is also demonstrated in the following way. By means of micro indentation, some microcracks are induced under a maximum load of 2 N at a loading speed of 14.4×10^{-2} N s^{-1} and a loading time of 10 seconds at maximum load. A very high percentage of transgranular fracture is present in the sinter-forged specimens (Fig. 12b), while almost only intergranular fractures take place in the pressureless sintered specimens (Fig. 12a). In the free sintered sample clearly weak grain boundaries and microcracks are present which was not the case for the sinter-forged samples. These results strongly suggest that the sinter forging process gives significant improvement of the grain boundary structure.

In conclusion the toughness of the compacts after sinter forging is mainly enhanced as a result of the improvement of the grain boundary structure. This results in an increase in fracture energy and consequently in an increase of grain-boundary toughness.

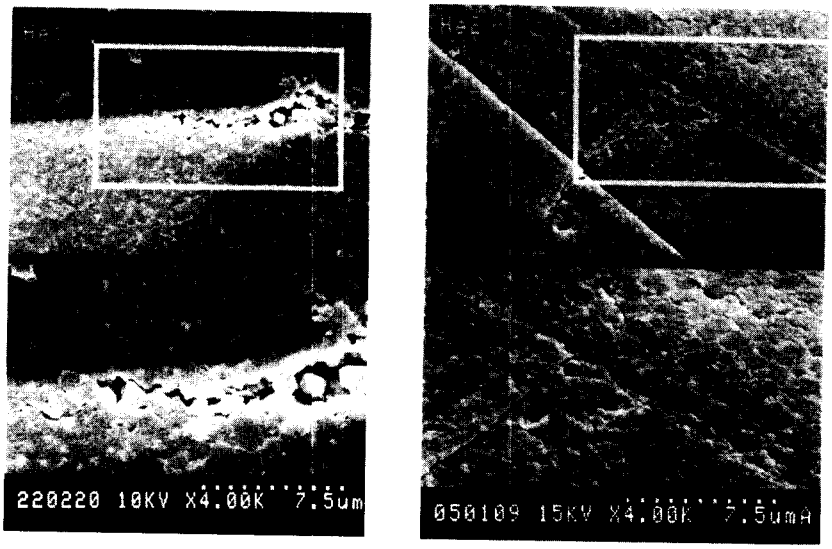

(a) (b)

Fig. 12. Features of the formation and propagation of cracks induced by a micro indentor under a maximum load of 2 N, a loading speed of 14.4×10^{-2} N s^{-1} and a holding time of 10 s.
(a) pressureless sintered, (b) sinter-forged.

11. Evaluation

In this chapter the state-of-the art on sinter forging of zirconia ceramics and zirconia-alumina composites has been given. In this section the most important findings will be summarized and some subjects for further modelling and research will be outlined.

Large creep strains can be imposed on zirconia ceramics during sinter forging, which makes it possible to prepare dense bodies at lower temperature and/or within shorter sintering times resulting in smaller grain sizes compared to free sintering. Sinter forging can be used as a forming technique for making near-net-shape bodies, especially in the case of fine-grained or nanocrystalline materials.

In pure zirconia almost no dynamic grain growth is observed. The presence of impurity (glassy) phases can however induce dynamic grain growth. In alumina-zirconia systems dynamic grain growth occurs only if the zirconia phase is not well distributed at multiple grain-junctions. Sinter forging of zirconia-alumina systems shows a special behaviour if a transition alumina phase (e.g. θ - alumina) is present in the green compact. The rearrangement of the particles under stress during the (reconstructive) phase transformation results in an optimal microstructure for further densification.

Large flaws introduced during green state forming can be removed during sinter forging by the applied strain. Moreover, the growth of smaller flaws to large ones during sintering is suppressed. These phenomena lead to a strong improvement of strength and reliability. Creep occurs by grain-boundary sliding during sinter forging. Shearing of the grain boundaries during grain switching reinforces the grain boundary network. Grain boundary microcracks and "more open" grain boundaries are eliminated. Amorphous grain-boundary phases are removed from boundaries under

compression during sinter-forging. Even crystallization of this glassy phase might occur. This all indicates that not only densification is improved and flaw concentrations are diminished by sinter forging, but also grain boundaries are "improved" in this way. The concept of grain-boundary toughness needs more attention. Analysis of the grain-boundary morphology by techniques like TEM, in combination with EDX and surface analysis techniques such as XPS and Auger spectroscopy are useful for examining the change in grain-boundary properties by sinter forging.

Furthermore, the discrepancy between experimental data and theoretical models for the stress multiplication factor needs further research. Two major models (see Section 3) based on different concepts exist that give the dependence of the stress multiplication factor (ϕ) on porosity. Both models are complementary but experimentally observed values deviate significantly from the model predictions. Constitutive equations for densification during sinter forging as derived in this chapter are based on HIPing models. However, it is known that the addition of a deviatoric component to the hydrostatic pressure greatly accelerates densification. Explicit atomistic models should therefore be developed taking the deviatoric stresses into consideration to model densification during sinter forging.

12. References

[1] R.J. Raj, J. Am. Ceram. Soc. **70**, C-210 (1987)
[2] G. Skandan, H. Hahn, B.H. Kear, M. Roddy, W.R. Cannon, Materials Letters **20**, 305 (1994).
[3] A.G. Evans, J. Am. Ceram. Soc. **65**, 497 (1982).
[4] J.S. Reed, T. Carbone, C. Scott, Mater. Sci. Res. **11**, 171 (1978).
[5] K.R. Venkatachari and R.Raj, J. Am. Ceram. Soc. **70**, 514 (1987).
[6] P.C. Panda, J. Wang, R. Raj, J. Am. Ceram. Soc. **71**, C-507 (1988).
[7] R. Raj, J. Am. Ceram. Soc. **65**, C-46 (1982)
[8] B.J. Kellett and F. Lange, J. Am. Ceram. Soc. **71**, 7 (1988).
[9] B. Budiansky, J.W. Hutchinson and S. Slutsky, pp. 13-45 in: Mechanics of Solids. Edited by H.G. Hopkins and M.J. Sewell. Pergamon Press, NY, 1982.
[10] T.G. Nieh and J. Wadsworth, Scr. Metall. Mater. **24**, 763 (1990).
[11] A.H. Choksi and J.R. Porter, J. Am. Ceram. Soc. **70**, 197 (1987).
[12] C. Wolf, Ph.D. Thesis, TU Hamburg-Harburg, Fortschrittberichte VDI, Reihe 5, Nr. 386. VDI Verlag, Düsseldorf (1995).
[13] N. Claussen, private communication (1995).
[14] F. Wakai, S. Sakaguchi and Y. Matsuno, Adv. Cer. Mater. **1**, 259 (1986).
[15] P. Panda and E.R. Seydel, Am. Ceram. Soc. Bull. **65**, 338 (1986).
[16] K.R. Venkatachari and R. Raj, J. Am. Ceram. Soc. **69**, 499 (1986).
[17] M. Nauer, Ph. D. Thesis, EPF Lausanne, Switzerland (1992).
[18] M.M.R. Boutz, A.J.A. Winnubst and A.J. Burggraaf, J. Am. Ceram. Soc. **78**, 121 (1995).
[19] M.M.R. Boutz, R. Janßen and N. Claussen, to be published in Proceedings of ICCM-10, conference held at Whistler, Canada, August 14-18, 1995.
[20] M.N. Rahaman, L.C. de Jonghe and R.J. Brook, J. Am. Ceram. Soc. **69**, 53 (1986).
[21] P.D. Funkenbusch, W.J. Tseng and E.K.H. Li, pp. 631-37 in Ceramic Transactions Vol.12, Ceramic Powder Science III. Edited by G. Messing, S. Hirano and H. Hausner, American Ceramic Society, Westerville, Ohio (1990).
[22] W. Beere, J. Mater. Sci. **10**, 1434 (1975).
[23] R.L. Coble, J. Appl. Phys. **41**, 4798 (1970).
[24] W. Beere, Acta Metall. **23**, 131 (1975).
[25] W. Beere, Acta Metall. **23**, 139 (1975).
[26] J.M. Viera and R.J. Brook, J. Am. Ceram. Soc. **67**, 245 (1984).

[27] H.F. Fischmeier and E. Arzt, Powder Metall. **26**, 82 (1983).
[28] A.S. Helle, K.E. Easterling and M.F. Ashby, Acta Metall. **33**, 2163 (1985).
[29] R.L. Coble, J. Appl. Phys. **32**, 793 (1961).
[30] L.E. Murr, Chapter 3 in Interfactial Phenomena in Metals and Alloys. Addison Wesley, Reading, Massachusets, (1975).
[31] D.S. Wilkinson and M.F. Ashby, Acta Metall. **23**, 1277 (1975).
[32] D.S. Wilkinson and M.F. Ashby, pp. 67-76 in Science of Sintering, Vol.10, (1978).
[33] Y.S. Kwon, G. Son, J. Suh and K.T. Kim, J. Am. Ceram. Soc. **77**, 3137 (1994).
[34] M.M.R. Boutz "Nanostructured tetragonla zirconia ceramics; microstructure, sinter forging and superplasticity" Ph.D. thesis, university of Twente, The Netherlands (1993).
[35] A.J.A. Winnubst, M.M.R. Boutz, Y.J. He, A.J. Burggraaf, H. Verweij, pp. 1743-1754 in Ceramics: Charting the Future, ed. by P. Vincenzini, Techna Srl, Faenza, Italy (1995).
[36] M.M.R. Boutz, A.J.A. Winnubst, A.J. Burggraaf, M. Nauer, C. Carry, J. Eur. Ceram. Soc. **13**, 103 (1994).
[37] M. Nauer, C. Carry, Scripta Metall. Mater. **24**, 1459 (1990).
[38] Y.J. He, A.J.A. Winnubst, H.Verweij, A.J. Burggraaf, J. Mater. Sci. **29**, 6505 (1994)
[39] B.J. Kellet, F.F. Lange, J. Am. Ceram. Soc. **69**, (1986) C-172
[40] P. den Exter, A.J.A. Winnubst, T.H.P. Leuwerink, A.J. Burggraaf, J. Am. Ceram. Soc. **77**, 2376 (1994)
[41] M.J. Mayo, D.C. Hague, Mater. Sci. Forums, **170-172**, 141 (1994).
[42] M.M.R. Boutz, A.J.A. Winnubst, B. van Langerak, R.J.M. Olde Scholtenhuis, K. Kreuwel and A.J. Burggraaf, J. Mater. Sci. **30**, 1854 (1995).
[43] W. Weibull, J. Apll. Mech. **18**, 293 (1951).
[44] Y.J. He "Tribological and mechanical proeperties of fine-grained zirconia nad zirconia-alumina ceramics" Ph.D thesis, University of Twente, The Netherlands (1995).
[45] Y.J. He, A.J.A. Winnubst, C.D. Sagel-Ransijn, A.J. Burggraaf, H. Verweij, J. Eur. Ceram. Soc., **15**, 601 (1996).
[46] Y.J. He, A.J.A. Winnubst, H.Verweij, A.J. Burggraaf, J. Mater. Sci. **29**, 5868 (1994).
[47] Y.J. He, A.J.A. Winnubst, A.J. Burggraaf, H. Verweij. P.G.T. van der Varst, G. de With, J. Eur. Ceram. Soc., submitted (1996).
[48] H. Gleiter, pp. 15-21 in "1980 Deformation of Polycrystals", ed. N. Hansen, A. Horsewell, T. Leffers and L. Libholt, 2nd Risφ Int. Symp. on Metallurgy and Materials Science, Risφ Nat. Lab., Roskilde, Denmark, (1981).
[49] X. Xhu, R. Birringer, U. Herr, H. Gleiter, Phys. Rev. B. **35**, 9085 (1987).
[50] A. Krell and P. Blank, J. Eur. Ceram. Soc. **32**, 309 (1992).